

ARTICLE

Open Access

Development of plasmonic thin-layer chromatography for size-selective and optical-property-dependent separation of quantum dots

Tsukasa Torimoto¹, Naoko Yamaguchi¹, Yui Maeda¹, Kazutaka Akiyoshi¹, Tatsuya Kameyama¹, Tatsuya Nagai², Tatsuya Shoji^{2,3}, Hidemasa Yamane^{4,5}, Hajime Ishihara^{5,6,7} and Yasuyuki Tsuboi²

Abstract

Nano-objects, such as quantum dots (QDs), are essential units for the construction of functional materials and devices in current technologies. The establishment of a versatile scheme to sort desired components from a crude product is crucial for bringing out the full potential of the original materials. However, it is still challenging to separate QDs with the same composition on the basis of size and to sort QDs with the same size but different optical properties. Here, we demonstrate such sorting for the first time by combining plasmonic optical trapping with thin-layer chromatography (TLC), which is a widely used tool. LED photoexcitation of the localized surface plasmon resonance of Au nanoparticles immobilized on a TLC plate affected the distance QDs traveled depending on the wavelength and intensity of irradiated light, which led to clear separation according to the size and/or optical properties of the QDs. Since optical property-based separation cannot be achieved by conventional chromatography, in which the interactions between stationary phases of chromatographs and QDs are simply based on differences in the size or surface functionality of the QDs, the present strategy will be a key solution for the establishment of a versatile scheme for sorting nano-objects.

Introduction

Optical manipulation is a nondestructive and non-invasive technique based on the use of a focused laser to apply an optical force on micro- and nanoscale particles, and it has attracted much attention for various applications, such as crystallization of organic molecules, sorting of nanomaterials, and cell manipulation^{1–12}. Optical manipulation has been an important technology for the selective transportation of nano-objects since the optical force on nanoparticles is dependent on their shape and size as well as their optical properties. Imasaka et al. developed a new technique called optical chromatography

in which polymer microspheres 1~6 μm in size are optically sorted under flow in a microcapillary by coaxially irradiating counterpropagating laser light¹³. Ajiki et al. proposed chirality-selective optical sorting of single-walled carbon nanotubes (SWCNTs)¹⁴, and this technique was experimentally demonstrated by Spesyvtseva et al., who showed that the optical scattering force was increased by the resonant condition between the electronic transitions of SWCNTs and the wavelength of laser light, resulting in an increase in the transport rate of SWCNTs with a particular chirality¹⁵. Dholakia and coworkers successfully controlled the diffusion direction of gold nanoparticles of different sizes (100~150 nm) by using counterpropagating evanescent waves of different wavelengths¹⁶. Fujiwara et al. reported that nanodiamonds were driven along a nanofiber by optical forces induced by two counterpropagated lasers, and the direction was dependent on the presence or absence of

Correspondence: Tsukasa Torimoto (torimoto@chembio.nagoya-u.ac.jp) or Yasuyuki Tsuboi (twoboys@osaka-cu.ac.jp)

¹Graduate School of Engineering, Nagoya University, Chikusa-ku, Nagoya 464-8603, Japan

²Graduate School of Science, Osaka City University, 3-3-138 Sugimoto, Sumiyoshi, Osaka 558-8585, Japan

Full list of author information is available at the end of the article

© The Author(s) 2022



Open Access This article is licensed under a Creative Commons Attribution 4.0 International License, which permits use, sharing, adaptation, distribution and reproduction in any medium or format, as long as you give appropriate credit to the original author(s) and the source, provide a link to the Creative Commons license, and indicate if changes were made. The images or other third party material in this article are included in the article's Creative Commons license, unless indicated otherwise in a credit line to the material. If material is not included in the article's Creative Commons license and your intended use is not permitted by statutory regulation or exceeds the permitted use, you will need to obtain permission directly from the copyright holder. To view a copy of this license, visit <http://creativecommons.org/licenses/by/4.0/>.

nitrogen-vacancy centers in the diamonds¹⁷. Recently, the use of plasmonic optical trapping for manipulating nanoscale objects has also been intensively investigated. An intense electric field was formed by the excitation of localized surface plasmon resonance (LSPR) at peaks of metal nanostructures and the optical force acted on nano-objects^{18–21}. The advantages of plasmonic trapping are that it can reduce the intensity of incident laser light by several orders of magnitude, and it can trap target objects in a nanometer-scale area near metal nanostructures. For example, Tsuboi and coworkers demonstrated plasmonic trapping of CdSe quantum dots of ca. 10 nm in size on gold nanodimer arrays²². Since optical manipulations, even plasmonic optical trapping, have generally been performed in micrometer-scale areas under optical microscopes, it is currently quite challenging to apply optical manipulation for treating or sorting nano-objects in a larger area, such as an area of a few cm² or larger.

Among the various kinds of nano-objects, semiconductor nanocrystals, so-called quantum dots (QDs), have attracted much attention for various applications, such as applications in optoelectronic devices, photoluminescence materials, and photocatalysts, because they exhibit unique physicochemical properties that are tunable by their size and chemical composition^{23–27}. Less toxic multinary QDs, such as AgInS₂, Cu(In,Ga)S₂, and their solid solutions with other semiconductors^{28–37}, have been intensively investigated as an alternative to conventional highly toxic binary QDs, such as CdSe and PbS. Since colloiddally synthesized QDs have a certain size distribution, narrowing their distribution has been an important postsynthetic treatment for improving their performance. Various strategies for precisely separating QDs by size have been developed³⁸. The strategies include size-selective precipitation³⁹, electrophoresis^{40,41}, and size-exclusion chromatography^{42–45}, which are based on the size dependence of the solubility of QDs in solution, surface charge, and incorporation into mesopores of the stationary phase, respectively. Unlike binary QDs, however, multinary QDs exhibit different energy gaps depending on their chemical composition even if their particle sizes are the same. Thus, a novel strategy is needed for the separation of QDs by optical properties as well as by size.

Here, we propose a unique strategy for the size-selective separation of QDs by combining plasmonic trapping with thin-layer chromatography (TLC), a strategy we named “plasmonic TLC”. TLC techniques are well known as relatively inexpensive techniques used in laboratories to investigate the purity of chemicals, monitor the progress of a reaction and isolate chemical species. Au nanoparticles (NPs) as plasmonic materials were immobilized on TLC plates. LSPR photoexcitation of Au NPs decreased the traveling distance of QDs as an analyte on

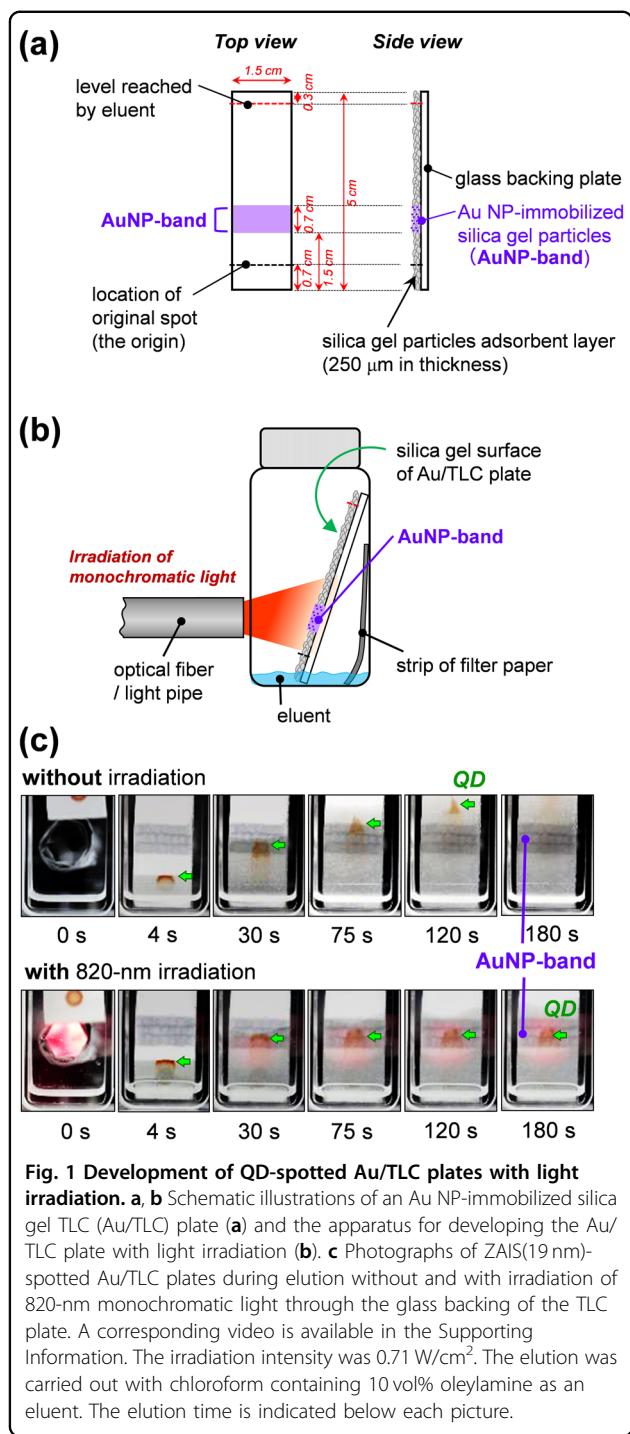
TLC plates, and the degree was dependent on the irradiation intensity. The QDs were captured according to their size and/or light absorption property in the area of Au NPs loaded on TLC plates by light irradiation with an intensity larger than a threshold value. The plasmonic TLC performance was influenced by the wavelength of irradiated light: The selection of monochromatic lights, enabling photoexcitation of both target QDs and the LSPR of Au NPs, decreased the irradiation intensity to capture QDs. Plasmonic TLC will be a useful strategy for relatively large-scale applications to select nano-objects with differences in their absorption properties as well as their sizes.

Results and discussion

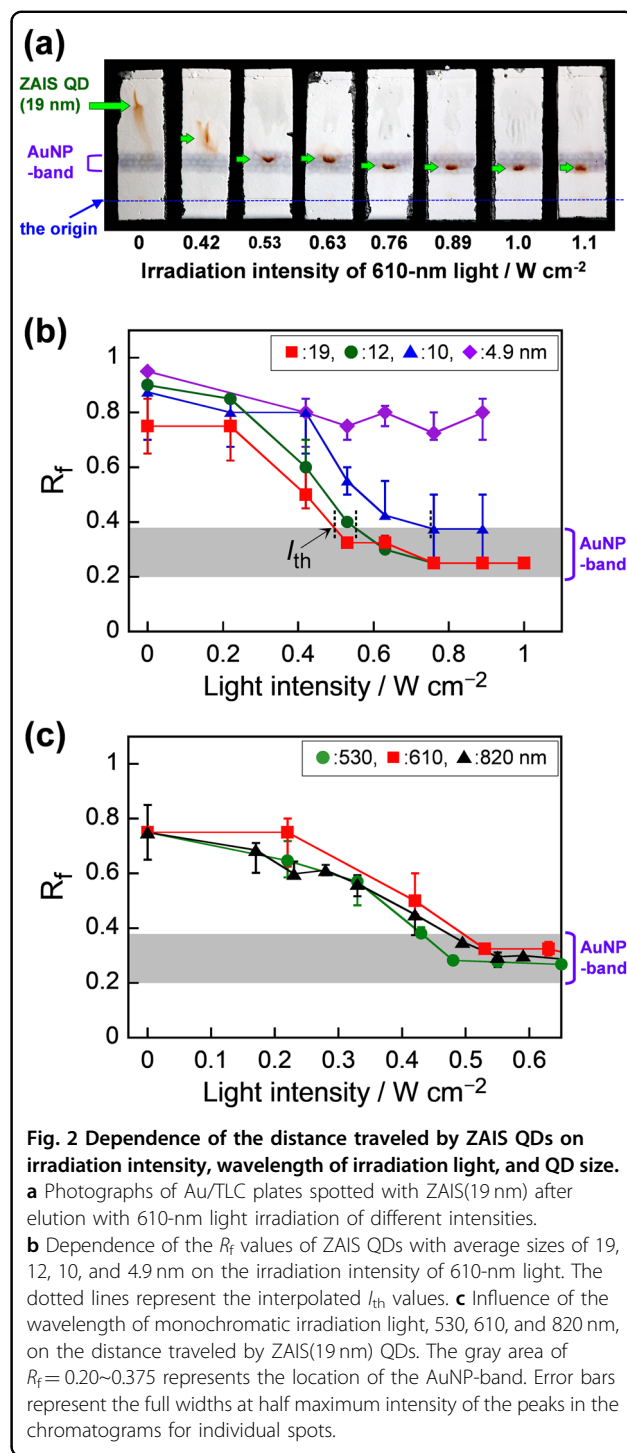
Trapping of QDs with LSPR photoexcitation

We spread an aqueous solution containing Au NPs (size: 12 nm) on a silica gel particle layer as the stationary phase of a TLC plate to form a band-like Au NP-immobilized area (AuNP-band) (Fig. 1a). Although Au NPs exhibited a narrow LSPR peak at 520 nm in an aqueous solution, loading Au NPs on TLC plates produced a broad LSPR peak in the wavelength range from 500 to >1800 nm, as shown in Fig. S1a. The peak top was located at ~670 nm on the longer wavelength side of that of Au NPs in solution. This broad peak was assignable to a gap-mode LSPR of aggregated Au NPs. SEM measurements (Fig. S2) revealed that Au NPs were not uniformly immobilized on the silica gel particle surface but formed large aggregates of ca. 200 nm in size on the gently curved surfaces of flake-like silica gel particles in the stationary phase of the TLC plate.

Droplets of a chloroform solution of Zn-Ag-In-S QDs 19 nm in size (ZAIS(19 nm)) (Fig. S3) were placed at the origin of Au/TLC, followed by development with chloroform containing oleylamine (10 vol%) as an eluent (Fig. 1b). The pictures in Fig. 1c show how the ZAIS QD spots traveled during the development of Au/TLC plates with or without irradiation by monochromatic light at 820 nm with an intensity of 0.71 W/cm². The corresponding video is available in the Supporting Information (Movie S1). The AuNP-band in Au/TLC was stable while the eluent traveled up the silica gel stationary phase on the plates by capillary action. As the eluent rose and migrated across an original brown spot, the QD spot traveled upward and went through the AuNP-band without light irradiation, as generally expected. In contrast, we observed unique behavior with 820-nm irradiation of the AuNP-band. Although the eluent rose in a similar manner and passed through the AuNP-band on the TLC plate, the QD spot was trapped in the AuNP-band. However, irradiation of TLC plates with 820-nm light of the same intensity could not stop the QD spot from traveling in the absence of the AuNP-band.



Irradiation with 610-nm light effectively photoexcited the LSPR peak of Au NPs loaded on TLC plates, as did the 820-nm light irradiation (Fig. S1). The irradiation intensity affected the distance traveled by the ZAIS(19 nm) on Au/TLC plates, as shown in Fig. 2a. Irradiation with 610-nm light with an intensity of 0.53 W cm⁻² or higher resulted in the trapping of QDs in the AuNP-band. The light irradiation did not decompose the QDs or



irreversibly immobilize the QDs on the surface of the Au/TLC plates because the second development of the QDs trapped in the AuNP-band of Au/TLC without irradiation enabled the QD spot to migrate across the AuNP-band (Fig. S4). From photographs of the TLC plates, we extracted a profile of the brightness level for ZAIS QDs as a chromatogram using Image-J software and determined

the position of the spot of QDs as a peak top in the profile to calculate the R_f value, which was defined as the ratio of the distance traveled by the QDs to the distance of the eluent front from the origin. Figure 2b shows the relationship between the R_f values of ZAIS QDs with various sizes and the irradiation intensity of 610-nm light; error bars represent the full widths at half maximum intensity of the peaks in the chromatograms for individual spots. The light intensity dependence of R_f was strongly influenced by the sizes of the QDs. Regardless of the QD size, the R_f value of the ZAIS QDs decreased with increasing light intensity. Although QDs of 4.9 nm in size passed through the AuNP-band regardless of the light intensity, QDs with sizes larger than 10 nm were trapped in the AuNP-bands with irradiation intensities larger than the threshold values, I_{th} . By drawing a straight line between the nearest plots for each kind of QD, we interpolated the I_{th} value to give $R_f = 0.375$, which corresponded to the value of the upper border of the AuNP-band. The obtained I_{th} values decreased from 0.75 to 0.55 and to 0.50 W/cm² with an increase in QD size from 10 to 12 and to 19 nm, respectively. Similar behavior of QD trapping on Au/TLC plates with irradiation was observed when various kinds of solvents, including toluene and octane, were used as eluents.

The light intensity dependence of the R_f value also varied depending on the wavelength used for irradiation. Figure 2c shows the R_f values of ZAIS(19 nm) QDs as a function of the irradiation intensity of monochromatic light with different wavelengths, 530, 610, and 820 nm. The distance traveled by ZAIS(19 nm) decreased with increasing irradiation intensity in each case. The I_{th} values were dependent on the wavelength, and the values determined by interpolation were 0.43, 0.50, and 0.47 W/cm² for irradiation at 530, 610, and 820 nm, respectively. A broad LSPR peak of the Au/TLC plate gave similar values of the Kubelka-Munk (K-M) function at 610 and 820 nm, which were 0.23 and 0.22, respectively (Fig. S1). In the present case, we can assume that the K-M function is proportional to the intensity of the LSPR peak of Au NPs immobilized on TLC plates. Thus, these results suggested that similar degrees of LSPR excitation of the AuNP-band gave similar QD trapping efficiencies, resulting in the observation of analogous I_{th} values for the irradiation wavelengths at 610 and 820 nm. However, since the K-M function of Au/TLC was 0.18 at 530 nm, the photoexcitation of LSPR of the AuNP-band at 530 nm was not as effective as that with photoexcitation at 610 and 820 nm, and we expected that the I_{th} value would become larger for 530-nm light irradiation. However, this was not true in the present case. Instead, the 530-nm irradiation induced more efficient optical trapping of QDs with an I_{th} value that was ca. 10% smaller than the values with 610-nm and 820-nm irradiation. The fact that

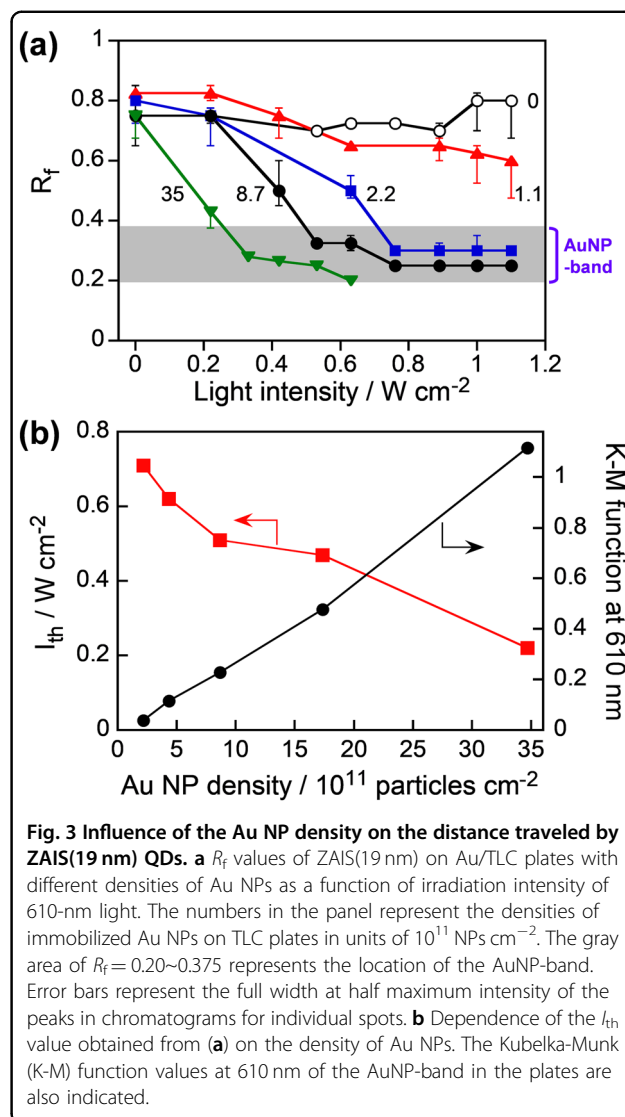


Fig. 3 Influence of the Au NP density on the distance traveled by ZAIS(19 nm) QDs. **a** R_f values of ZAIS(19 nm) on Au/TLC plates with different densities of Au NPs as a function of irradiation intensity of 610-nm light. The numbers in the panel represent the densities of immobilized Au NPs on TLC plates in units of 10^{11} NPs cm⁻². The gray area of $R_f = 0.20\text{--}0.375$ represents the location of the AuNP-band. Error bars represent the full width at half maximum intensity of the peaks in chromatograms for individual spots. **b** Dependence of the I_{th} value obtained from (a) on the density of Au NPs. The Kubelka-Munk (K-M) function values at 610 nm of the AuNP-band in the plates are also indicated.

ZAIS(19 nm) QDs with an energy gap (E_g) of 1.96 eV were significantly photoexcited by 530-nm light but not by 610-nm light or 820-nm light (Fig. S3) suggested that the change in the absorption property of the QDs affected their migration rates across the AuNP-band.

The TLC performance can be controlled by the LSPR peak intensity of the AuNP-band. Figure 3a shows the R_f values of ZAIS(19 nm) on Au/TLC plates with different Au NP densities as a function of the intensity of 610-nm light irradiation. By using Au/TLC plates with a Au NP density $<1.1 \times 10^{11}$ NPs cm⁻², ZAIS(19 nm) QDs could not be trapped in the AuNP-band with light irradiation at any of the intensities investigated. However, Au/TLC plates with Au NP densities of 2.2×10^{11} NPs cm⁻² or larger successfully captured the QDs by light irradiation at higher intensities. The I_{th} values were interpolated from Fig. 3a and plotted in Fig. 3b, in which the K-M function

values of the Au/TLC plates (Fig. S5) were also plotted. With an increase in Au NP density, the I_{th} value gradually decreased from 0.71 to 0.22 W/cm², accompanied by a linear increase in the K-M function of the AuNP-band. These results indicated that the trapping efficiency of QDs in the AuNP-band was tunable by adjusting the intensity of the LSPR electric field formed around Au NPs through modulation of the irradiation light intensity and/or by varying the density of photoexcited Au NPs that served as trapping sites.

Another factor to be considered is a temperature increase (ΔT) on Au/TLC by LSPR photoexcitation. We estimated the local temperature increase from temperature-sensitive dye fluorescence⁴⁶ (see Supporting Information) and found that the photoexcitation of Au/TLC plates caused a ΔT of 1.1 K with an increase in the 808-nm laser intensity by 1.0 kW cm⁻² for LSPR photoexcitation (Fig. S6). Even when the plates were irradiated with monochromatic light with an intensity of 1 W cm⁻² or less, we concluded that the temperature change of Au/TLC was negligible in the present study.

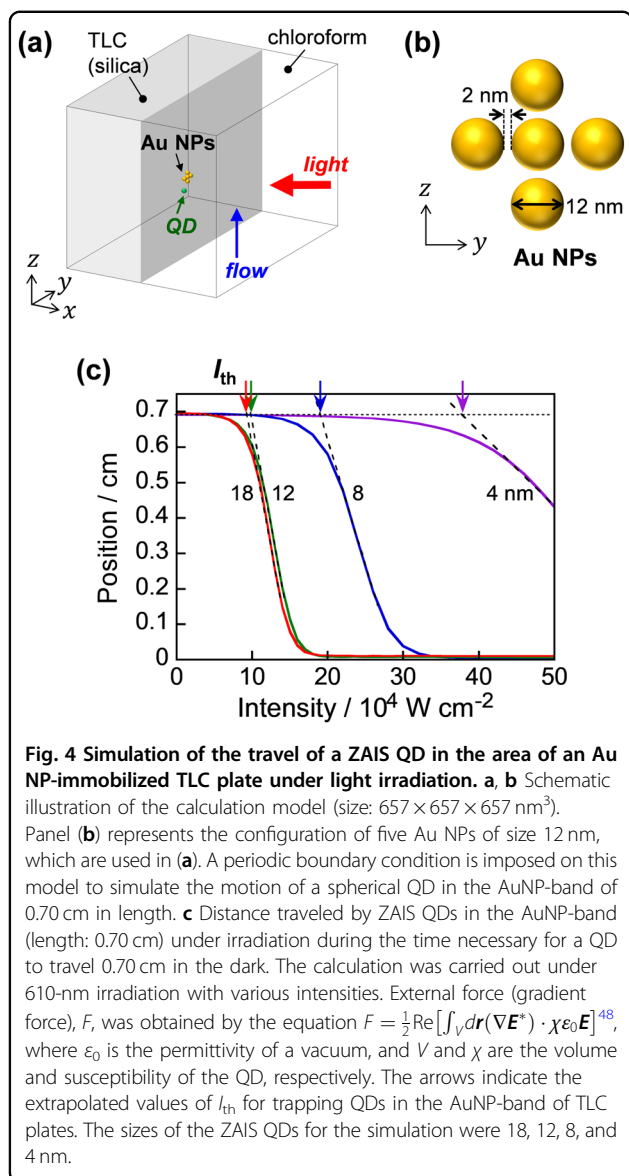
Adsorption of a target component on the stationary phase is one of the important parameters needed for separating a mixture of chemical species into their components with TLC. To clarify the mechanism of trapping in the AuNP-band with light irradiation, we investigated the adsorption strength of ZAIS QDs of different sizes on silica gel particles in chloroform eluent solution. The amount of QDs adsorbed on silica gel particles, S_{ad} , gradually increased with increasing concentration of QDs in the solution, C_s , and finally seemed to reach a plateau (Fig. S7). By assuming a Langmuir adsorption isotherm for the adsorption behavior of QDs, we estimated the adsorption constant, K_{ad} , of QDs on silica gel particles. The K_{ad} values increased with increased QD size and were determined to be 1.1×10^7 , 6.8×10^7 , and 6.3×10^8 dm³ mol⁻¹ for ZAIS(4.9 nm), ZAIS(10 nm) and ZAIS(19 nm) (Table S1), respectively. Since the obtained K_{ad} values were relatively large, $10^7 \sim 10^8$ dm³ mol⁻¹, we assumed that most of the QDs were adsorbed on silica gel particles as a stationary phase in the TLC plate, regardless of their size.

Thus, we can propose a mechanism of QD trapping with the plasmonic TLC technique. Photoexcitation of the LSPR peak of Au NPs on the TLC plate results in the formation of a locally enhanced electric field in the proximity of Au NPs, which produces an attractive force (F) between Au NPs and QDs via dipole–dipole interactions. The magnitude of F is roughly approximated as $F = \frac{1}{2} \Re[\alpha] \nabla \langle E^2 \rangle$, where α is the polarizability of the target particle and is proportional to the particle volume, and E is the total response electric field of incident light^{3,47}. Adsorbed QDs can move in two dimensions on the silica gel surface and travel with the eluent by capillary action until they reach the LSPR-induced electric field around

Au NPs, where a significant attractive force between QDs and Au NPs retards the surface diffusion of QDs on silica gel particles. The magnitude of the attractive force increases with increasing polarizability of the QDs, that is, with an increase in the QD volume, as well as with an increase in the intensity of irradiated light to photoexcite the LSPR of Au NPs. As a result, larger QDs are trapped in the AuNP-band by a lower irradiation intensity.

We confirmed this hypothesis by model calculations of plasmonic trapping on a TLC plate. In this calculation, we examined the size dependence of the migration rates of QDs with respect to changes in the irradiation intensity. To elucidate the observed phenomena, we considered the following simple model. Namely, a small aggregate of Au NPs is immobilized on the surface of a silica plate immersed in a chloroform solution (Fig. 4a, b), and a ZAIS QD moves restrictedly in two dimensions on the silica surface. Assuming plane wave irradiation, we calculated the response field near the Au NPs by using the discrete dipole approximation (DDA) method. Using the resultant electric field, we estimated the optical force exerted on the QD⁴⁸. Then, based on the obtained force, we performed a simulation of the Brownian dynamics of the QD. Although the scattering force is induced by the direct irradiation of incident light on a QD, it is not necessary to consider its effect because the scattering force is perpendicular to the silica surface in this simulation and does not contribute to the movement of the QD (Fig. 4a). The QD is adsorbed on the silica surface and moves in two dimensions in a plane perpendicular to the direction to the incident light. In the real system, the scattering force is considered to be almost entirely canceled due to multiple scattering events inside the silica gel particle layer on the TLC plate. In the simulation, we took into account that the displacement of the QD due to Brownian motion decreases than that in the solvent due to the strong adsorption of the QD to the silica surface: the random force displacement, R_{ran} , is 1/100 of that of QDs freely dispersed in the solvent. The model and calculation method are described in detail in the Supporting Information (Fig. S8). Figure 4c shows the dependence of the traveling position of ZAIS QDs in the AuNP-band on the irradiation intensity. The I_{th} value, extrapolated from the linear region, increases with a decrease in the QD size, and the tendency is in good agreement with the experimental results (Fig. 2b).

We found that the light intensity that was necessary to plasmonically trap QDs in Fig. 2 was several orders of magnitude smaller than the I_{th} values in a previous study²², in which CdSe QDs of ca. 10 nm in size, uniformly dispersed in a solution, were optically trapped on an Au NP array with 808-nm laser irradiation at intensities of 0.5~10 kW/cm². The most important difference between the present study and the previous study is the



dimension of the diffusion of QDs. In the case of the present plasmonic TLC, QDs were adsorbed on the adsorbent (silica gel) particle layer on the TLC plate, and then the migration of QDs was confined in two dimensions on the surface of adsorbent particles, which is different from the previous case of using uniformly dispersed and freely diffused QDs in a solution. We clarified the importance of the adsorption of QDs by the simulation, as shown in Fig. S8b–d. The smaller the disturbance due to random force is as a result of the increase in the adsorption strength of the QD on the silica surface, the slower the migration rate of a QD for each size.

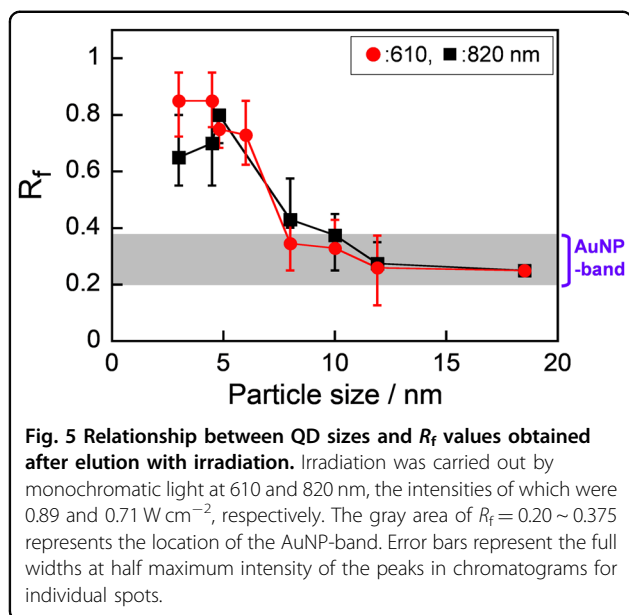
It should be noted that the photons originating from the photoluminescence (PL) of QDs and/or from the elastic light scattering by QDs can also excite LSPR of Au NPs to induce optical force. The QDs used in the present study

exhibited a relatively small PL quantum yield at 5~20%, and the contribution of PL to the optical force can thus be assumed to be small in comparison to that of direct LSPR excitation with irradiation light. Thus, we examined the contribution of the elastic light scattering by QDs, namely, we treated the optical response of the total system of QDs and AuNPs self-consistently. For the simulations shown in Fig. 4, we did not employ a self-consistent field for calculating force to avoid a heavy computational load. The electric field near the AuNPs on the TLC plate was obtained in the absence of QDs, and the force exerted on a QD at each point was estimated from the obtained electric field together with the QD polarizability. Figure S9 shows a comparison of the results obtained by non-self-consistent treatment (the same as Fig. 4) and self-consistent treatment for an 18-nm ZAIS QD with a y -polarized 610-nm laser. Although a QD feels a slightly stronger optical force in the case of the non-self-consistent treatment, it is clearly demonstrated that the contribution of the elastic light scattering by the QD to the magnitude of the force is not dominant in this case. Thus, we conclude that the non-self-consistent calculation, shown in Fig. 4, is an appropriate approximation method to understand the essence of the present experimental results.

With the present simulation, however, we cannot estimate the absolute value of the field intensity for QD trapping in plasmonic TLC in Fig. 2b. Possible factors for lowering I_{th} values are multiple light reflections causing the enhancement of the electric field by stacked silica gel particles, complicated surface diffusion of adsorbed QDs due to the surface roughness of individual silica gel particles and their stacking structure on TLC plates, and the hydrodynamic behavior of the eluent. These factors were not considered in the simulations to avoid an unrealistically long computational time. However, our results explain the essential tendency of the size dependence of QD migration by Au/TLC.

Size-selective separation of QDs with plasmon-photoexcited Au/TLC

We clarified the dependence of the R_f value on the QD size under light irradiation of constant intensity. The QDs used were ZAIS and Ag-In-Ga-S (AIGS) QDs of various sizes^{32,33,35}, the surfaces of which were modified with dodecanethiol. The E_{gs} of QDs, determined from the absorption onset, were in the range of 1.95~2.30 eV (Fig. S3), indicating that the QDs were slightly photoexcited by the 610-nm light but not by the 820-nm light. Without irradiation, each kind of QD traveled through the AuNP-band to give R_f values of approximately 0.7~0.9 (Fig. S10). In contrast, with irradiation of 610-nm light (0.89 W cm^{-2}) and 820-nm light (0.71 W cm^{-2}), QDs with sizes larger than the critical values, 8.0 and 10 nm,



respectively, were trapped in the AuNP-band (Fig. 5). It should be noted that the change in the critical size of trapped QDs with the wavelength of monochromatic light originated from the dependence of R_f values on the irradiation intensity shown in Fig. 2. This dependence of R_f on size motivated us to apply plasmonic TLC to QD size separation.

A QD mixture sample was prepared by blending rice-shaped ZAIS(19 nm) with a broad defect-site PL peak at approximately 700~800 nm and spherical AIGS(4.5 nm) showing a sharp band-edge PL peak at 530 nm (Fig. S3). This mixture solution showing two PL peaks at 530 and 740 nm was spotted onto Au/TLC plates, followed by development in a chloroform eluent solution with or without 820-nm irradiation. Without irradiation, the QD spot moved upward through the AuNP-band to form a smeared red spot at approximately $R_f = 0.7 \sim 0.95$ (Fig. S11), showing almost the same PL spectrum as that of the QD mixture (Fig. 6a). This indicated that mixed QDs were not size-selectively separated at all with conventional TLC. On the other hand, development with 820-nm light irradiation produced two spots at different R_f values, as shown in Fig. 6b. A red spot was trapped at $R_f = 0.25$ in the AuNP-band, while a blurred yellow spot appeared at $R_f = 0.6 \sim 0.95$. The former spot showed only a broad PL peak at approximately 700~800 nm assignable to that of ZAIS(19 nm) QDs, and the latter spot exhibited a sharp band-edge PL peak at 530 nm originating from AIGS(4.5 nm) (Fig. 6c). It should be noted that the spot at $R_f = 0.6 \sim 0.95$ also exhibited a broad PL peak at 630 nm that was assigned to defect-site emission because it was located at the longer wavelength side of the band-edge peak (530 nm). This is probably because surface defects

formed due to the partial removal of organic surface ligands from AIGS(4.5 nm) QDs during elution. To confirm the size-selective separation with Au/TLC under irradiation, a part of each spot and the underlying silica gel stationary phase were scraped from the developed Au/TLC plate, and the adsorbed QDs were extracted with chloroform to measure their size distribution by TEM. Although the original mixture exhibited a size distribution with two peaks at ca. 3~5 nm and ca. 15~22 nm (Fig. 6a), the QDs recovered from each spot had a unimodal size distribution (Fig. 6c). Only rice-shaped QDs with an average size of 17 nm were retrieved from the spot at $R_f = 0.25$, which were assigned to ZAIS(19 nm), and the spot at $R_f = 0.85$ contained only spherical QDs with a size of 4.1 nm that originated from AIGS(4.5 nm).

Size-selective separation was also carried out using a mixture of as-synthesized spherical, ellipsoidal, and dumbbell-shaped ZAIS QDs with sizes of 4~40 nm³⁶ (Fig. S12a). Under 610-nm light irradiation with 0.63 W cm^{-2} intensity, a large blurry spot appeared, spanning from $R_f = 0.45$ to 0.25 across the upper border of the AuNP-band (Fig. S12b). ZAIS QDs were recovered from the areas in the spot at $R_f = 0.4$ on a bare TLC plate and $R_f = 0.3$ on the AuNP-band. As shown in Fig. S12c, spherical or ellipsoidal QDs with sizes of 4~8 nm (average size: 4.6 nm) were observed at $R_f = 0.4$, while the AuNP-band trapped QDs with dumbbell and ellipsoidal shapes of size ca. 10 nm or larger (average size: 15 nm) at $R_f = 0.3$. The size limitation of QDs trapped in Au/TLC was ca. 8 nm, agreeing well with the results shown in Fig. 5. Such size-selective separation was not achieved without irradiation, where the QD spot was slightly streaked and then stopped at $R_f = 0.57$ (Fig. S12b).

Sorting QDs by their light absorption property

To precisely separate as-prepared QDs by size, most researchers have used size-selective precipitation³⁹, in which the addition of a nonsolvent selectively produced precipitates of larger QDs because of their relatively low solubility. However, this technique cannot be applied to the extraction of QDs of a target E_g from a mixture of QDs having the same sizes but different E_g s. Since it is well known that multinary QDs exhibit tunable light absorption properties in a wide wavelength region with respect to their chemical composition as well as with their particle size, the development of strategies for separating QDs according to their absorption properties is important but remains challenging. As mentioned above, it was suggested from Fig. 2c that the change in the absorption property of QDs affected their migration rates across the AuNP-band. This also suggests that the present plasmonic TLC technique enables sorting of QDs by their optical properties. Thus, we investigated the influence of the light absorption properties of rod-shaped QDs with

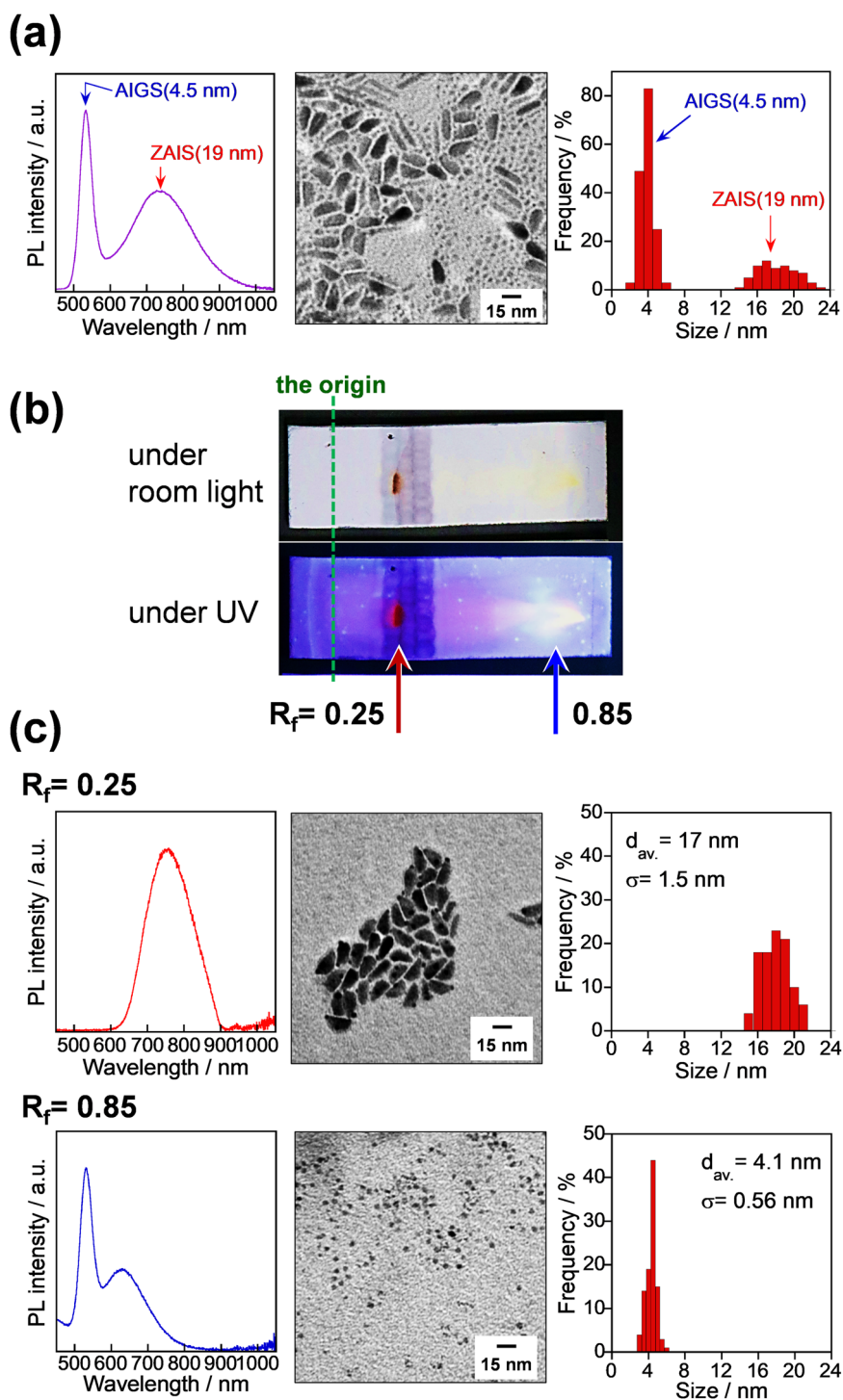
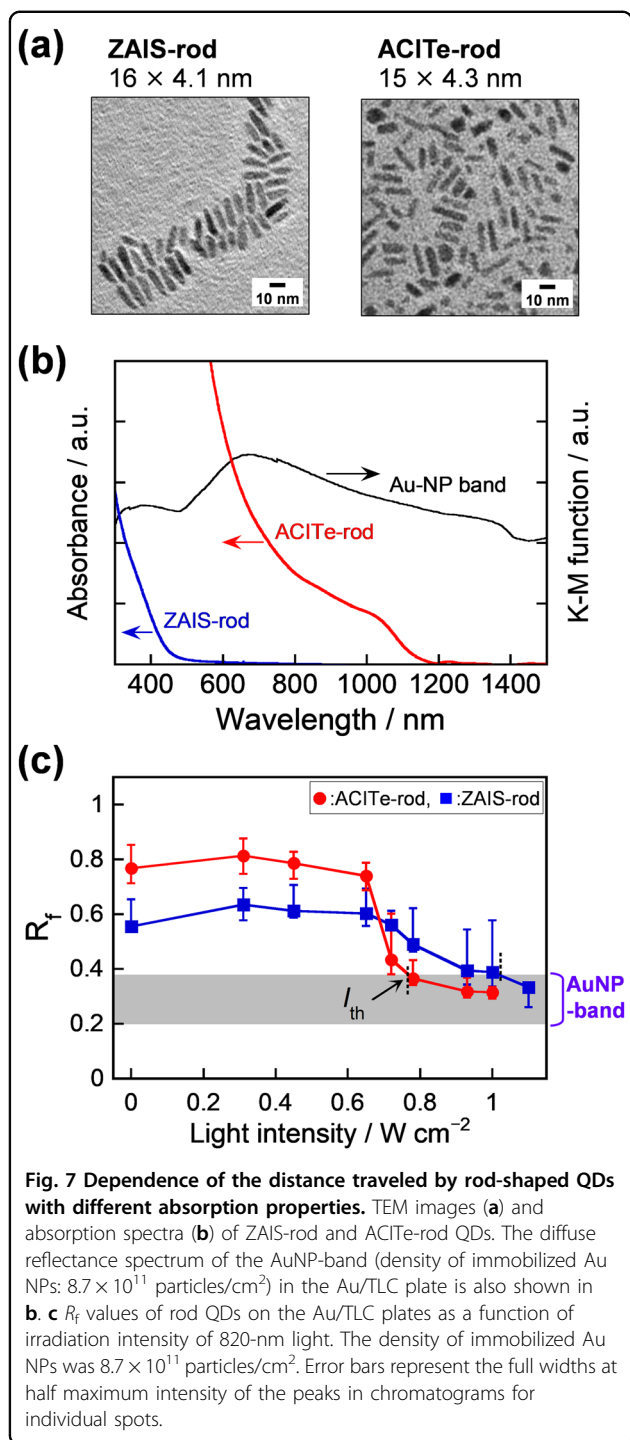


Fig. 6 Separation of QDs of different sizes from a mixture with Au/TLC. **a** PL spectrum, TEM image, and size distribution of the mixture of ZAIS(19 nm) and AIGS(4.5 nm). **b** Photographs of a QD-mixture-spotted Au/TLC plate after development with 820-nm light irradiation (intensity: 0.71 W cm^{-2}). The density of immobilized Au NPs was $8.7 \times 10^{11} \text{ particles/cm}^2$. **c** PL spectra of the spots at $R_f = 0.25$ and 0.85 on the developed Au/TLC plate (**b**) and TEM images and size distributions of QDs extracted from corresponding positions.



lengths of 15–16 nm and widths of ca. 4 nm, that is, ZAIS-rod and AgCuInTe (ACITe)-rod QDs (Fig. 7a, b), on the distance they travel when exposed to 820-nm light irradiation.

Since ZAIS-rod and ACITe-rod QDs had onsets of absorption spectra at 480 and 1150 nm, respectively, the 820-nm light irradiation for LSPR excitation of the

AuNP-band can photoexcite only ACITe-rod QDs during the development of Au/TLC plates (Fig. 7b). Without light irradiation, the R_f values obtained were ca. 0.6 for ZAIS-rod QDs and ca. 0.8 for ACITe-rod QDs. With an increase in the intensity of irradiation at 820 nm, the R_f values tended to decrease, and then both kinds of rod-shaped QDs were trapped in the AuNP-bands with irradiation intensities larger than the I_{th} values, which were interpolated to $1.02\ W\ cm^{-2}$ for ZAIS-rod QDs and ca. $0.77\ W\ cm^{-2}$ for ACITe-rod QDs. The I_{th} value of ACITe-rod QDs decreased compared to that of ZAIS-rod QDs. Since the 820-nm light effectively photoexcited ACITe-rod QDs in addition to the AuNP-band, the difference in the optical properties of the QDs caused remarkable differences in their migration rates across the AuNP-band. By using the calculation model shown in Fig. 4, we simulated the influence of the intensity of 820-nm irradiation on the distance traveled by two different kinds of spherical QDs (diameter of 8 nm) composed of ZAIS or ACITe, the absorption spectra of which were assumed to be the same as those shown in Fig. 7b. At an incident light wavelength of 820 nm, the real parts of the susceptibilities of the ACITe and ZAIS QDs were obtained as 11.0 and 0.634, respectively, using the relative permittivity ϵ_r , estimated from the experimental data of the absorption spectra, $\chi = \epsilon_r - 1$. The polarizabilities are defined by susceptibilities and volume of QDs; $\alpha = \chi V / \epsilon_0$, where ϵ_0 represents the permittivity of a vacuum and V and χ are the volume and susceptibility of the QDs, respectively. QDs are attracted by the gradient force arising from LSPR in the vicinity of Au NPs. This slows the speed of the migration of QDs in the TLC, as shown in Fig. S13. Since this optical force (gradient force) is proportional to the real part of the polarizability of the QD, the migration speed depends on the optical properties of the QD. The I_{th} values were obtained in the simulation from the relationship between the distance traveled by a QD and the irradiation intensity (Fig. S13). ACITe QDs exhibited a smaller I_{th} value than that obtained for ZAIS QDs. This tendency agreed with the results shown in Fig. 7c, although the simulated values were much greater than the experimentally obtained values, similar to the difference between the results shown in Figs. 2b and 4c.

To compare the magnitude of the optical force depending on the absorption property of the QD, we obtained maps of the forces acting on each QD in Fig. S14 under 820-nm light irradiation with the intensity at I_{th} for the ACITe QD in Fig. S13. Their line profiles are shown in Fig. S15. The difference in the force map originated from the magnitude of the real part of the polarizability of QDs. By integrating the forces in the y - z plane, we obtained maps of the potential, U , of the optical force field for 8-nm ACITe and ZAIS QDs. Assuming that the diffusion distance R_{ran} on the TLC plate is g times that of Brownian

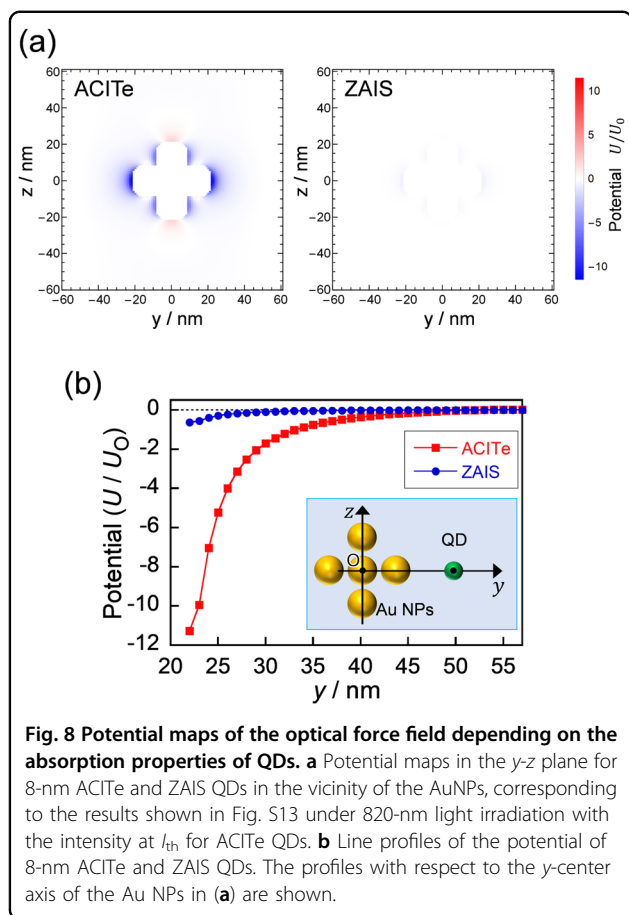


Fig. 8 Potential maps of the optical force field depending on the absorption properties of QDs. **a** Potential maps in the y - z plane for 8-nm ACITe and ZAIS QDs in the vicinity of the AuNPs, corresponding to the results shown in Fig. S13 under 820-nm light irradiation with the intensity at I_{th} for ACITe QDs. **b** Line profiles of the potential of 8-nm ACITe and ZAIS QDs. The profiles with respect to the y -center axis of the Au NPs in (a) are shown.

motion in the solvent because of the adsorption effect, the diffusion energy can be estimated as $U_0 = kT/g^2$ (see Supplementary Information). The potential maps normalized by the diffusion energy without irradiation (U_0) are shown in Fig. 8, where we set $g = 1/100$, corresponding to Fig. S13 in the Supplementary Information. Regardless of the kind of QDs, the potential becomes lower with decreasing distance between the QD and the aggregate of Au NPs, but the magnitude of the potential decrease is larger for ACITe QDs than for ZAIS QDs because of a larger value of the real part of the polarizability. These results indicate that an ACITe QD can be more easily optically trapped near Au NPs at the intensity of I_{th} for ACITe, overcoming diffusion, while a ZAIS QD is not captured.

Figure 7c suggests that ACITe-rod QDs were selectively captured in the AuNP-band if a mixture of these QDs was eluted on Au/TLC under 820-nm irradiation with intensities in the range of $0.77 \sim 1.02 \text{ W cm}^{-2}$. To confirm this hypothesis, we prepared a mixture by blending ZAIS-rod and ACITe-rod QDs with a particle number ratio of 80:20 (Fig. S16). This mixture was not separated into the two kinds of original QDs by a conventional size-selective precipitation method. Droplets of the solution containing the

mixture of QDs were placed onto Au/TLC plates, followed by development in a chloroform eluent solution under 820-nm irradiation of 0.78 W cm^{-2} intensity. A dark-brown spot was trapped at $R_f = 0.27$ in the AuNP-band on the developed TLC plate (upper panel of Fig. 9a), and a yellow PL spot was seen at $R_f = 0.46$ under UV light (lower panel of Fig. 9a). Figure 9b shows the diffuse reflectance spectrum and PL spectrum of each spot. The spot at $R_f = 0.27$ exhibited broad absorption in the visible and near-IR wavelength regions, and the absorption onset was observed ca. 1000 nm, which was assigned to the ACITe-rod QDs (Fig. 7b). Considering that ZAIS-rod QDs had an intense PL peak at 580 nm (Fig. S3), no PL peak appeared for the spot at $R_f = 0.27$, indicating that the trapped QDs were composed of pure ACITe-rod QDs. However, the spot at $R_f = 0.46$ had almost no absorption in the range of 400–800 nm but showed a PL peak at 580 nm, indicating the presence of only ZAIS-rod QDs. A part of each spot with the underlying silica gel stationary phase was scraped from the developed plate, and then the trapped QDs were extracted with chloroform to measure their size distribution by TEM. Rod-shaped QDs were observed at individual spots, as also shown in Fig. 9b, and their size distributions were almost the same, with average values (length \times width) of $15 \times 4.0 \text{ nm}$ and $16 \times 4.5 \text{ nm}$ for QDs at $R_f = 0.27$ and 0.46 , respectively. A dark-brown spot and a yellow PL spot passed through the AuNP-band in the case of development of the Au/TLC plate without irradiation and then stopped at $R_f = 0.90$ and 0.49 on the Au/TLC plate (not shown), respectively, which were in rough agreement with the R_f values of the corresponding pure samples (Fig. 7c). Thus, we concluded that the present plasmonic TLC strategy enables optical-property-dependent separation of QDs even when target QDs have a particle size and a morphology that are almost the same as those of other QDs in the mixture such as a byproduct or contaminant.

Conclusions

We successfully developed a novel plasmonic TLC technique for the separation of QDs by coupling conventional TLC plates and Au NPs as plasmonic materials. Monochromatic incoherent light of relatively weak intensity, such as LED light, enabled the plasmonic TLC to be driven. We successfully separated QDs from a mixture of QDs using this strategy. Although QDs $< 6 \text{ nm}$ in size were not trapped at any of the irradiation intensities investigated, QDs 8 nm or larger in size strongly adsorbed on the adsorbent layer on the TLC plate and were captured in the band-like Au NP-immobilized area by LSPR photoexcitation with a light intensity of ca. $0.5 \sim 1 \text{ W/cm}^2$, which was several orders of magnitude less than that previously reported for plasmonic trapping of QDs uniformly dispersed in a solution with Au NP arrays²². The two-dimensional surface diffusion of QDs plays an important

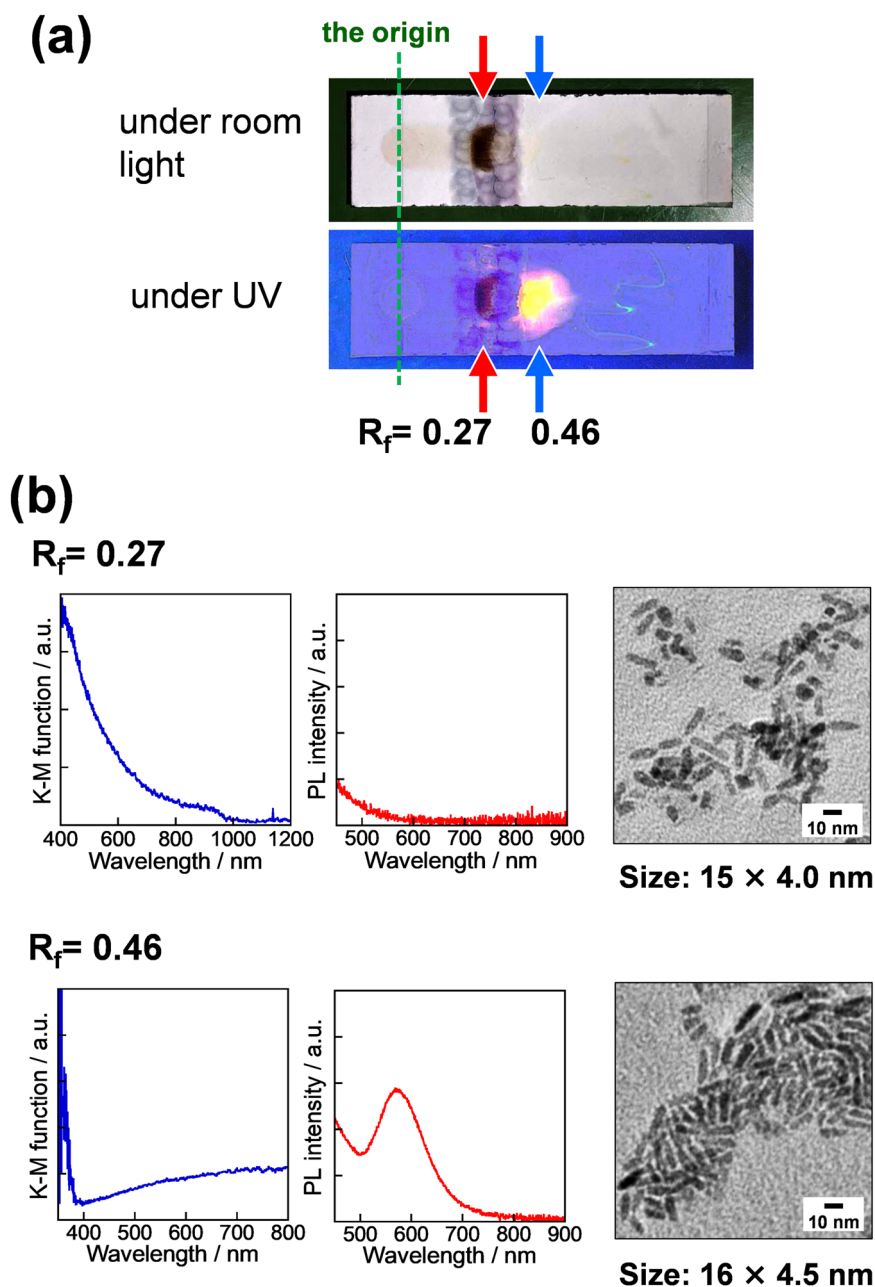


Fig. 9 Isolation of target QDs from a mixture according to their absorption property. **a** Photographs of spots of a QD-mixture on an Au/TLC plate after development with 820-nm light irradiation (intensity: 0.78 W cm^{-2}). The QD mixture contained ZAIS-rod and ACITE-rod QDs with a particle number ratio of 80:20 (Fig. S16). The density of Au NPs immobilized on the TLC plate was 8.7×10^{11} particles/cm². **b** Diffuse reflectance spectra (left) and PL spectra (middle) of the spots at $R_f = 0.27$ and 0.46 on the developed Au/TLC plate. TEM images of QDs extracted from corresponding positions are also shown (right).

role in their capture using plasmonic optical trapping in the present strategy. Theoretical simulations confirmed that the migration rates of target QDs were retarded by the attractive forces between LSPR-excited Au NPs and QDs adsorbed on the stationary phase, the magnitude of which was dependent on their size. Furthermore, we found that differences in the optical properties of QDs affected their

trapping efficiency in the AuNP-band, enabling the sorting of QDs of similar sizes by the difference in their optical properties. The essence of the selectivity according to the optical properties of QDs can be theoretically understood on the basis of the change in the attractive forces acting on QDs in the LSPR-electric field (induced by the incident light) with the difference in the real part of the polarizability

of QDs. Our findings and the underlying mechanism will be important for developing a novel strategy for the separation of QDs with similar sizes but different optical properties. Such optical property-based separation cannot be achieved by conventional chromatography, where the interactions between stationary phases of chromatographs and QDs are simply based on the differences in the size or surface functionality of QDs. In the near future, plasmonic TLC will become another useful strategy for separating nano-objects, such as metal nanocrystals, quantum dots, polymers, vesicles, and biomolecules, by optical properties as well as size.

Methods

Silica gel TLC plates (Anal Tech, stationary phase: 15- μm silica gel particles with 60 Å pores, layer thickness: 250 μm , C18-hydrocarbon-impregnated (5%)) were cut into pieces of 5.0 cm in length \times 1.5 cm in width and used as substrates for the immobilization of Au NPs. An aqueous dispersion of Au NPs (size: 12 nm) was uniformly spread in the band area, 0.7 \times 1.5 cm, on a TLC plate with a height of 1.5–2.2 cm from the plate bottom (AuNP-band, Fig. 1a), followed by drying under vacuum. The NP density of the AuNP-band was 8.7×10^{11} NPs cm^{-2} , unless otherwise noted. The thus-obtained plates are denoted here as Au/TLC plates. A line was drawn as the origin of TLC with a pencil 0.70 cm from the TLC plate bottom. The Au/TLC plates were immersed for ca. 5 min in chloroform containing 5 vol% oleylamine to remove impurities adsorbed on the plates, followed by drying.

Multinary QDs with various sizes, including Zn-Ag-In-S (ZAIS) QDs of 4.9, 8.0, 10, 12 and 19 nm in size and Ag-In-Ga-S (AIGS) QDs with sizes of 3.0, 4.5, and 6.0 nm, were prepared by previously reported procedures^{32,33,35} with slight modification (details in the Supporting Information) and were dissolved in chloroform. We used the abbreviations ZAIS(size) and AIGS(size) to refer to QDs with different sizes. The concentration of QDs in a solution for spotting was typically 1.4×10^{-6} mol(QDs) dm^{-3} . A 4.0-mm³ portion of the QD chloroform solution was applied to the origin of the Au/TLC plate, with the size of the round spot typically being 0.3–0.4 cm in diameter. After drying the spot, the Au/TLC plate was placed in a development chamber (screw-capped glass vial, 3 cm in diameter \times 6.5 cm in height) with chloroform containing 10 vol% oleylamine as an eluent. Until the eluent front reached ca. 0.30 cm below the top of the TLC plate, monochromatic light (Fig. S1b) was directly irradiated on the AuNP-band from the silica gel surface of the TLC plate, except when recording a video of Au/TLC development, in which case the irradiation passed through the glass backing of the TLC plate. The monochromatic light sources used for irradiation were a red LED unit (CCS Inc., PFBR-150RD) for 610-nm light, a green LED unit

(CCS Inc., PFBR-150GR) for 530-nm light, and a 300-W Xe lamp light (EAGLE, CX-05E) through near-IR band-pass filters (SIGMAKOKI, ITF-50S-83RT and SCF-50S-64R) for 820-nm light. The experimental setup is shown in Fig. 1b. The eluent was allowed to travel 4.0 cm from the origin, that is, to 0.30 cm below the top of the TLC plate, and as a result, the AuNP-band was located in the area of $R_f = 0.20\sim 0.375$ after development.

Acknowledgements

This work was supported by JSPS KAKENHI Grant Numbers JP16H06504 and JP16H06507 in Scientific Research on Innovative Areas "Nano-Material Optical-Manipulation", JP18H03927, JP20K05558, JP20H02550, JP21K14554, JP21K14703, JP21H05019 and JP22H00341. T.K. thanks PRESTO, JST for financial support (Grant Number JPMJPR18T5). Y.T. is grateful to the CANON Foundation.

Author details

¹Graduate School of Engineering, Nagoya University, Chikusa-ku, Nagoya 464-8603, Japan. ²Graduate School of Science, Osaka City University, 3-3-138 Sugimoto, Sumiyoshi, Osaka 558-8585, Japan. ³Department of Chemistry, Faculty of Science, Kanagawa University, 2946 Tsuchiya, Hiratsuka 259-1293, Japan. ⁴Department of Physics, Kitasato University, 1-15-1, Kitazato, Minami-ku, Sagami-hara, Kanagawa 252-0373, Japan. ⁵Department of Physics and Electronics, Osaka Prefecture University, 1-1 Gakuen-cho, Naka-ku, Sakai, Osaka 599-8531, Japan. ⁶Department of Materials Engineering Science, Osaka University, 1-3 Machikaneyama-cho, Toyonaka, Osaka 560-8531, Japan. ⁷Center for Quantum Information and Quantum Biology, Osaka University, 1-1 Yamadaoka, Suita, Osaka 565-0871, Japan

Author contributions

T.T., H.I., and Y.T. conceived the plasmonic TLC technique. N.Y., Y.M., K.A., T.K., and T.T. prepared QDs with different sizes and investigated the plasmonic TLC performance of Au/TLC with the use of these QDs. T.N., T.S., and Y.T. carried out the measurements of changes in the local temperature of Au/TLC with irradiation. H.Y. and H.I. simulated the diffusion of QDs on Au/TLC. T.T., H.I., and Y.T. wrote this paper. All authors discussed the results and commented on the manuscript.

Conflict of interest

The authors declare no competing interests.

Publisher's note

Springer Nature remains neutral with regard to jurisdictional claims in published maps and institutional affiliations.

Supplementary information The online version contains supplementary material available at <https://doi.org/10.1038/s41427-022-00414-3>.

Received: 19 February 2022 Revised: 13 May 2022 Accepted: 24 May 2022.
Published online: 22 July 2022

References

- Ashkin, A. & Dziedzic, J. M. Optical trapping and manipulation of viruses and bacteria. *Science* **235**, 1517–1520 (1987).
- Zhang, H. & Liu, K.-K. Optical tweezers for single cells. *J. R. Soc. Interface* **5**, 671–690 (2008).
- Bendix, P. M., Jauffred, L., Norregaard, K. & Oddershede, L. B. Optical trapping of nanoparticles and quantum dots. *IEEE J. Sel. Top. Quantum Electron.* **20**, 4800112 (2014).
- Lehmuskero, A., Johansson, P., Rubinsztein-Dunlop, H., Tong, L. & Käll, M. Laser trapping of colloidal metal nanoparticles. *ACS Nano* **9**, 3453–3469 (2015).
- Zemanek, P., Volpe, G., Jonas, A. & Brzobohaty, O. Perspective on light-induced transport of particles: from optical forces to phoretic motion. *Adv. Opt. Photonics* **11**, 577–678 (2019).

6. Favre-Bulle, I. A., Stilgoe, A. B., Scott, E. K. & Rubinsztein-Dunlop, H. Optical trapping in vivo: theory, practice, and applications. *Nanophotonics* **8**, 1023–1040 (2019).
7. Bustamante, C., Alexander, L., Maciuba, K. & Kaiser, C. M. Single-molecule studies of protein folding with optical tweezers. *Annu. Rev. Biochem.* **89**, 443–470 (2020).
8. Corsetti, S. & Dholakia, K. Optical manipulation: advances for biophotonics in the 21st century. *J. Biomed. Opt.* **26**, 070602 (2021).
9. Gieseler, J. et al. Optical tweezers - from calibration to applications: a tutorial. *Adv. Opt. Photonics* **13**, 74–241 (2021).
10. Ishihara, R. Optical manipulation of nanoscale materials by linear and non-linear resonant optical responses. *Adv. Phys. -X* **6**, 1885991 (2021).
11. Kolbow, J. D., Lindquist, N. C., Ertsgaard, C. T., Yoo, D. & Oh, S.-H. Nano-optical tweezers: methods and applications for trapping single molecules and nanoparticles. *ChemPhysChem* **22**, 1409–1420 (2021).
12. Masuhara, H. & Yuyama, K.-i. Optical force-induced chemistry at solution surfaces. *Annu. Rev. Phys. Chem.* **72**, 565–589 (2021).
13. Imasaka, T., Kawabata, Y., Kaneta, T. & Ishidzu, Y. Optical chromatography. *Anal. Chem.* **67**, 1763–1765 (1995).
14. Ajiki, H., Iida, T., Ishikawa, T., Uryu, S. & Ishihara, H. Size- and orientation-selective optical manipulation of single-walled carbon nanotubes: a theoretical study. *Phys. Rev. B* **80**, 115437 (2009).
15. Spesyvtseva, S. E. S., Shoji, S. & Kawata, S. Chirality-selective optical scattering force on single-walled carbon nanotubes. *Phys. Rev. Appl.* **3**, 044003 (2015).
16. Ploschner, M., Cizmar, T., Mazilu, M., Di Falco, A. & Dholakia, K. Bidirectional optical sorting of gold nanoparticles. *Nano Lett.* **12**, 1923–1927 (2012).
17. Fujiwara, H., Yamauchi, K., Wada, T., Ishihara, H. & Sasaki, K. Optical selection and sorting of nanoparticles according to quantum mechanical properties. *Sci. Adv.* **7**, eabd9551 (2021).
18. Juan, M. L., Righini, M. & Quidant, R. Plasmon nano-optical tweezers. *Nat. Photonics* **5**, 349–356 (2011).
19. Kotsifaki, D. G. & Chormaic, S. N. Plasmonic optical tweezers based on nanostructures: fundamentals, advances and prospects. *Nanophotonics* **8**, 1227–1245 (2019).
20. Ghosh, S. & Ghosh, A. Next-generation optical nanotweezers for dynamic manipulation: from surface to bulk. *Langmuir* **36**, 5691–5708 (2020).
21. Ren, Y. et al. Plasmonic optical tweezers for particle manipulation: principles, methods, and applications. *ACS Nano* **15**, 6105–6128 (2021).
22. Tsuboi, Y. et al. Optical trapping of quantum dots based on gap-mode-excitation of localized surface plasmon. *J. Phys. Chem. Lett.* **1**, 2327–2333 (2010).
23. Hines, D. A. & Kamat, P. V. Recent advances in quantum dot surface chemistry. *ACS Appl. Mater. Interfaces* **6**, 3041–3057 (2014).
24. Pietryga, J. M. et al. Spectroscopic and device aspects of nanocrystal quantum dots. *Chem. Rev.* **116**, 10513–10622 (2016).
25. Moon, H., Lee, C., Lee, W., Kim, J. & Chae, H. Stability of quantum dots, quantum dot films, and quantum dot light-emitting diodes for display applications. *Adv. Mater.* **31**, 1804294 (2019).
26. Melnychuk, C. & Guyot-Sionnest, P. Multicarrier dynamics in quantum dots. *Chem. Rev.* **121**, 2325–2372 (2021).
27. Kagan, C. R., Bassett, L. C., Murray, C. B. & Thompson, S. M. Colloidal quantum dots as platforms for quantum information science. *Chem. Rev.* **121**, 3186–3233 (2021).
28. Chen, B., Pradhan, N. & Zhong, H. From large-scale synthesis to lighting device applications of ternary III-VI semiconductor nanocrystals: inspiring greener material emitters. *J. Phys. Chem. Lett.* **9**, 435–445 (2018).
29. Moodelly, D., Kowalik, P., Bujak, P., Pron, A. & Reiss, P. Synthesis, photophysical properties and surface chemistry of chalcopyrite-type semiconductor nanocrystals. *J. Mater. Chem. C* **7**, 11665–11709 (2019).
30. Berends, A. C., Mangnus, M. J. J., Xia, C., Rabouw, F. T. & Donega, C. D. M. Optoelectronic properties of ternary III-VI₂ semiconductor nanocrystals: Bright prospects with elusive origins. *J. Phys. Chem. Lett.* **10**, 1600–1616 (2019).
31. Kapuria, N. et al. Metal chalcogenide semiconductor nanocrystals synthesized from ion-conducting seeds and their applications. *J. Mater. Chem. C* **8**, 13868–13895 (2020).
32. Kameyama, T. et al. Controlling the electronic energy structure of ZnS-AgInS₂ solid solution nanocrystals for photoluminescence and photocatalytic hydrogen evolution. *J. Phys. Chem. C* **119**, 24740–24749 (2015).
33. Torimoto, T. et al. Controlling shape anisotropy of ZnS-AgInS₂ solid solution nanoparticles for improving photocatalytic activity. *ACS Appl. Mater. Interfaces* **8**, 27151–27161 (2016).
34. Uematsu, T. et al. Narrow band-edge photoluminescence from AgInS₂ semiconductor nanoparticles by the formation of amorphous III-VI semiconductor shells. *NPG Asia Mater.* **10**, 713–726 (2018).
35. Kameyama, T. et al. Wavelength-tunable band-edge photoluminescence of nonstoichiometric Ag-In-S nanoparticles via Ga³⁺ doping. *ACS Appl. Mater. Interfaces* **10**, 42844–42855 (2018).
36. Kameyama, T., Koyama, S., Yamamoto, T., Kuwabata, S. & Torimoto, T. Enhanced photocatalytic activity of Zn-Ag-In-S semiconductor nanocrystals with a dumbbell-shaped heterostructure. *J. Phys. Chem. C* **122**, 13705–13715 (2018).
37. Yamanishi, J. et al. Optical force mapping at the single-nanometre scale. *Nat. Commun.* **12**, 3865 (2021).
38. Shen, Y., Gee, M. Y. & Greytak, A. B. Purification technologies for colloidal nanocrystals. *Chem. Commun.* **53**, 827–841 (2017).
39. Murray, C. B., Norris, D. J. & Bawendi, M. G. Synthesis and characterization of nearly monodisperse CdE (E = S, Se, Te) semiconductor nanocrystallites. *J. Am. Chem. Soc.* **115**, 8706–8715 (1993).
40. Eychmuller, A., Katsikas, L. & Weller, H. Photochemistry of semiconductor colloids. 35. Size separation of colloidal CdS by gel electrophoresis. *Langmuir* **6**, 1605–1608 (1990).
41. Lhuillier, E., Hease, P., Ithurria, S. & Dubertret, B. Selective electrophoretic deposition of CdSe nanoplatelets. *Chem. Mater.* **26**, 4514–4520 (2014).
42. Fischer, C. H., Weller, H., Katsikas, L. & Henglein, A. Photochemistry of colloidal semiconductors. 30. HPLC investigation of small CdS particles. *Langmuir* **5**, 429–432 (1989).
43. Krueger, K. M., Al-Somali, A. M., Falkner, J. C. & Colvin, V. L. Characterization of nanocrystalline CdSe by size exclusion chromatography. *Anal. Chem.* **77**, 3511–3515 (2005).
44. Roberge, A., Dunlap, J. H., Ahmed, F. & Greytak, A. B. Size-dependent PbS quantum dot surface chemistry investigated via gel permeation chromatography. *Chem. Mater.* **32**, 6588–6594 (2020).
45. Suess, S. et al. Chromatographic property classification of narrowly distributed ZnS quantum dots. *Nanoscale* **12**, 12114–12125 (2020).
46. Shoji, T. et al. Optical tweezing and binding at high irradiation powers on black-Si. *Sci. Rep.* **7**, 12298 (2017).
47. Shoji, T. & Tsuboi, Y. Plasmonic optical tweezers toward molecular manipulation: tailoring plasmonic nanostructure, light source, and resonant trapping. *J. Phys. Chem. Lett.* **5**, 2957–2967 (2014).
48. Iida, T. & Ishihara, H. Theory of resonant radiation force exerted on nanostructures by optical excitation of their quantum states: from microscopic to macroscopic descriptions. *Phys. Rev. B* **77**, 245319 (2008).